Annals of Biomedical Engineering (© 2017)
DOI: 10.1007/s10439-017-1839-z

An MRI-Guided Telesurgery System Using a Fabry-Perot Interferometry Force Sensor and a Pneumatic Haptic Device

HAO SU,[1] WEIJIAN SHANG,[2] GANG LI,[2] NIRAVKUMAR PATEL,[2] and GREGORY S. FISCHER[2]

[1]Wyss Institute for Biologically Inspired Engineering and the John A. Paulson School of Engineering and Applied Sciences, Harvard University, Cambridge, MA 02138, USA; and [2]Automation and Interventional Medicine Robotics Laboratory, Department of Mechanical Engineering, Worcester Polytechnic Institute, 100 Institute Road, Worcester, MA 01609, USA

(*Received 8 October 2016; accepted 20 April 2017*)

Associate Editor Xiaoxiang Zheng oversaw the review of this article.

Abstract—This paper presents a surgical master-slave teleoperation system for percutaneous interventional procedures under continuous magnetic resonance imaging (MRI) guidance. The slave robot consists of a piezoelectrically actuated 6-degree-of-freedom (DOF) robot for needle placement with an integrated fiber optic force sensor (1-DOF axial force measurement) using the Fabry-Perot interferometry (FPI) sensing principle; it is configured to operate inside the bore of the MRI scanner during imaging. By leveraging the advantages of pneumatic and piezoelectric actuation in force and position control respectively, we have designed a pneumatically actuated master robot (haptic device) with strain gauge based force sensing that is configured to operate the slave from within the scanner room during imaging. The slave robot follows the insertion motion of the haptic device while the haptic device displays the needle insertion force as measured by the FPI sensor. Image interference evaluation demonstrates that the telesurgery system presents a signal to noise ratio reduction of less than 17% and less than 1% geometric distortion during simultaneous robot motion and imaging. Teleoperated needle insertion and rotation experiments were performed to reach 10 targets in a soft tissue-mimicking phantom with 0.70 ± 0.35 mm Cartesian space error.

Keywords—MRI-compatible robot, MR-conditional, Image-guided surgery, Percutaneous interventions, Haptics, Teleoperation.

INTRODUCTION

The last decade produced an expansion of magnetic resonance imaging (MRI)-guided robotics and several prototypes have been developed for different interventional procedures, including the shape memory actuated neurosurgical robot by Ho *et al.*,[8] the piezoelectrically actuated stereotactic neurosurgery robot by Su *et al.*,[11] the pneumatic robot for aortic valve replacement by Li *et al.*,[12] the pneumatically actuated concentric tube robot[3] by Comber *et al.* and the novel MRI-powered actuator for tissue biopsy by Dupont *et al.*,[6] among others.

Certain MRI-guided robotic systems have progressed through clinical trials in animals or humans such as.[1,10,21,23] Nevertheless, due to the formidable cost of MRI which is proportional to the imaging duration, the accumulated evidence and lessons from those clinical trials have revealed that it is imperative to minimize procedure time and thus reduce cost[21] to facilitate widespread adoption of this technique in additional hospitals. An MRI-guided procedure is time consuming because it typically requires imaging of the patient inside the MRI bore, followed by alignment and placement of the interventional tools outside the bore, and finally moving the patient into the bore for confirmation. Although some robotic devices (e.g.,[2,19]) are capable of aligning tools inside the bore, the insertion step is typically performed manually outside the bore resulting in a procedure that is still iterative and time-consuming.

One promising approach to tackling this issue is the use of a telesurgical system. In terms of human-robot interaction, surgical robots can be classified into three broad categories, namely, supervisory-controlled systems, telesurgical systems and shared-control systems.[13] The majority of MRI-guided surgical robots are clustered in the first category, in which the surgeon plans the operation, and then the robot performs the specified motion autonomously or semi-autonomously. In shared-control systems, the surgeon and robot

Address correspondence to Hao Su, Wyss Institute for Biologically Inspired Engineering and the John A. Paulson School of Engineering and Applied Sciences, Harvard University, Cambridge, MA 02138, USA. Electronic mails: haosu.ieee@gmail.com, gfischer@wpi.edu

Published online: 26 April 2017

control the surgical instrument collaboratively and synergistically; often with a hands-on interface. Telesurgical systems allow manual manipulation of a master robot to control a slave robot that performs the interventional procedure. Thus, the surgeon maintains intuitive control of the procedure, and the slave robot is able to remain inside the scanner bore to avoid iterative imaging (inside-bore) and intervention (outside-bore) processes.

Despite its merits, the telesurgical system for MRI-guided interventions is technically challenging because it requires the meticulous design of MRI-compatible master/slave robotic systems and a haptic user interface. In a telesurgical system, the surgeon will not directly operate the interventional tools (e.g., needles, forceps, *etc.*) as the manual approach, thus the tactile sensation of tool manipulation is lost. To regain this feedback to make the interventional procedure safe and intuitive, one solution is to mount force sensors at the distal portion to measure the insertion force and use haptic device to display it to the user. One stringent requirement is that both the force sensor and haptic device should be compatible with the MRI environment in order to maintain the proximity of the physician to the patient during the intervention. Several groups have reported the development of MRI-compatible master-slave systems. Kokes *et al.*[9] evaluated a teleoperated hydraulic needle driver robot with a commercially available DC motor-based haptic interface (PHANTOM OMNI, Geomagic Inc., USA) that is not MRI-compatible and must be located outside the MRI room. To ameliorate image quality deterioration, the same group[24] developed a 4-degrees-of-freedom (DOF) breast biopsy robot that consists of a pneumatically actuated parallel mechanism (3 DOF), a piezoelectrically actuated needle driver (1 DOF) and an intensity-based fiber-optic sensor. However, the position tracking performance of pneumatic actuation is typically mediocre due to nonlinear friction inside the pneumatic cylinders and nonlinear dynamics caused by the long pneumatic hose.[25] Seifabadi *et al.* evaluated the position tracking accuracy of a teleoperated needle insertion robot without haptic feedback, while Tse *et al.*[22] developed a haptic system with piezoelectric motors and proposed neural network-based admittance force control.

Through our previous research effort, we have tackled the MRI-compatibility issue of piezoelectric actuators by the development of the custom piezoelectric actuator driver that fundamentally minimizes the image artifact caused by actuation systems.[19] Commercially available piezoelectric motor drivers typically use amplification systems that generate the waveforms by low-pass filtering high-frequency square waves. By using switching drivers, significant RF emissions and noise on the motor drive lines are introduced which cause interference with imaging.[10] Although filtering can improve the results, it has not been effective in eliminating the interference and often significantly degrades motor performance. In Ref. 19, we presented our implementation of a piezoelectric motor driver with signals generated from a direct digital synthesizer, high-performance multichannel digital-to-analog converter, high power linear amplifiers, and π filtered outputs.

Leveraging this piezoelectric actuation control method, we have developed the slave robot[19] of the presented telesurgery system. It is a 6-DOF needle placement mechatronic system that consists of a 3-DOF needle driver module and a 3-DOF Cartesian motion module. The needle driver provides cannula translation and rotation (2-DOF) and stylet translation (1-DOF).[19]

Since the telesurgical system incorporates extra electromechanical components (FPI sensors and pneumatic haptic device) and teleoperation control algorithm besides the slave robot, this paper proposes a telesurgical system that optimizes the three key aspects of a master-slave teleoperation system, namely, sensing, haptic interface and control. First, by leveraging our expertise in MRI-compatible piezoelectric actuation that minimizes signal-to-noise ratio (SNR) reduction,[19] we further developed a Fabry-Perot Interferometry (FPI)-based highly sensitive sensor for needle insertion force sensing (1-DOF axial force). Second, we have developed a pneumatic haptic device with strain gauge force sensing for intuitive control of needle rotation and insertion. Third, we presented an impedance control-based bilateral teleoperation control method and demonstrated slave-side position tracking and master-side force tracking capabilities. This is the first archival publication on the use of FPI and piezoelectric actuation in an MRI-guided slave robot and pneumatic actuation for a haptic device with a successful teleoperation tracking demonstration inside an MRI scanner room. Some results in this manuscript appeared in preliminary conference paper form in Ref. 18. We presented the MRI compatibility evaluation using the signal-noise ratio metric and targeting accuracy characterization of the slave robot in Ref. 19. Notable additions and extensions of this paper include Fabry-Perot interferometry force sensor design optimization and calibration, MRI compatibility evaluation, force and position tracking of the master/slave telesurgery system.

MATERIALS AND METHODS

To ensure the MRI compatibility of the master-slave telesurgical system, this section presents the sys-

tem architecture, design of the FPI force sensor for needle insertion force sensing of the slave robot and the pneumatic haptic device. Then it presents the force and position control of the master-slave system.

System Architecture and Workflow

The system architecture is illustrated in Fig. 1. From the master robot side, the surgeon manipulates the pneumatic master robot (haptic device) to control the needle placement. From the slave side, the FPI fiber-optic force sensor measures the needle insertion force and reflects it back to the surgeon through the haptic device. To ensure safety and accessibility to the patient, the surgeon operates the master-slave teleoperation system from within the MRI scanner room with visualization of the interventional procedure through real-time MRI.

To minimize disruption to the traditional workflow, the teleoperation workflow mimics the traditional TransRectal UltraSound (TRUS)-guided biopsy, the current gold standard. This workflow is primarily composed of two phases (supervisory and teleoperation phases) and three key steps (Fig. 2): preparation, registration and planning, and targeting and verification.[17]

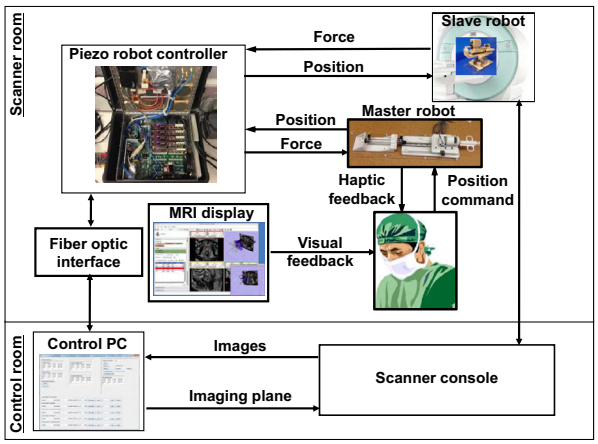

FIGURE 1. System architecture of the master-slave teleoperation system. The slave robot resides inside the MRI scanner bore, and the haptic device and piezo robot controller are located inside the MRI room. The control computer is located in the console room and is linked *via* fiber-optic bidirectional communication with the controller.

Fabry-Perot Fiber Optic Sensor for Insertion Force Sensing on Slave Robot

In Ref. 19, we developed a 6-DOF fully actuated needle placement slave robot. The needle driver of the slave robot offers two co-axial insertion translations and an axial rotation for tissue biopsy and brachytherapy. To regain the tactile sensation of the needle insertion force in a teleoperation scheme, we aim to measure an axial insertion force of up to 20 N because a typical prostate intervention force does not exceed 18 N.[26] We are the first group to deploy an FPI sensor for MRI-guided robotic prostate interventions. This approach was chosen because FPI offers high sensitivity (resolution 0.01% of full scale) and its signal conditioning (voltage measurement) is much simpler than that of wavelength-based fiber Bragg grating (FBG) sensors.

The phase-modulated fiber-optic force sensor offers displacement sensing through voltage measurement induced by a relative phase shift between light beams.

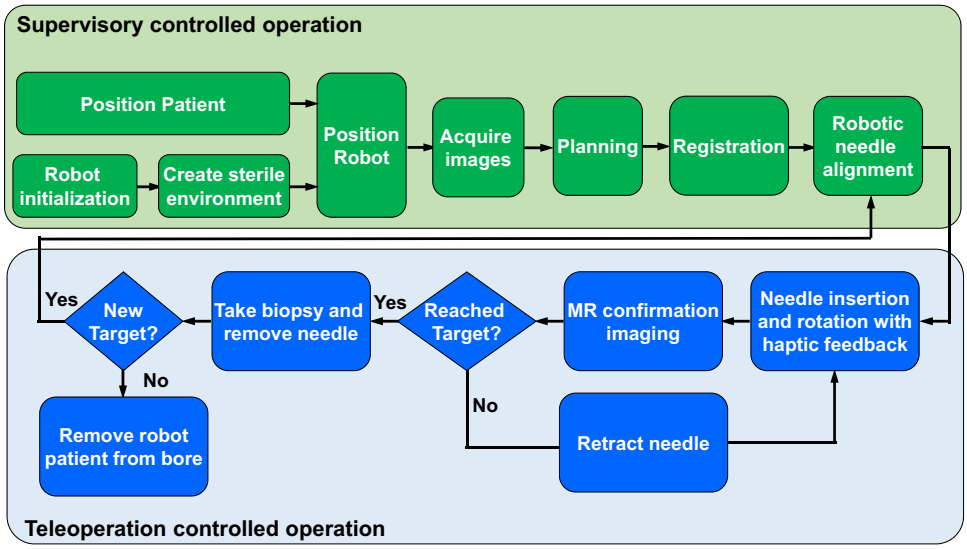

FIGURE 2. Teleoperation control workflow consisting of supervisory controlled operation and teleoperation controlled operation phases. The three key steps are preparation, registration and planning, and targeting and verification.

When an external force is applied, the length of the Fabry-Perot cavity L_{cavity} changes by δ. Therefore, the incident light follows a different light pathway, causing a phase difference $\Delta\phi$ (changed from ϕ_1 to ϕ_2). When the reflected light is focused using a lens, the interference fringes form concentric circles. The intensity of the fringes is calculated using the principle[7]:

$$I = A_1^2 + A_2^2 + 2A_1A_2\cos(\phi_1 - \phi_2) \quad (1)$$

with A_1 and A_2 representing the amplitude coefficients of the two reflected light sources. By substituting $A_i^2 = I_i (i = 1, 2)$ and $\phi_1 - \phi_2 = \Delta\phi$, this equation can be represented by the intensity and phase difference

$$I = I_1 + I_2 + 2\sqrt{I_1 I_2}\cos\Delta\phi \quad (2)$$

Based on beam mechanics, the bending force F induces a strain:

$$\varepsilon_{xx} = \frac{12FLc}{bt^3E} \quad (3)$$

where L is the length of the beam, c is the distance from the center of the beam in the y-direction (horizontal direction), b and t are the beam width and thickness, respectively, and E is Youngs modulus.

The phase change $\Delta\phi$ is equal to the wave number $\frac{2\pi}{\lambda}$ multiplied by the length of the sensing cavity region and the strain in the x-direction:

$$\Delta\phi = \frac{2\pi L_{cavity}\varepsilon_{xx}}{\lambda} \quad (4)$$

Substituting the phase change into the intensity equation, the output intensity becomes a function of the induced strain:

$$I = I_1 + I_2 + 2\sqrt{I_1 I_2}\cos\left(\frac{2\pi L_{cavity}\varepsilon_{xx}}{\lambda}\right) = I + A\cos(k\varepsilon_{xx}) \quad (5)$$

where I, A and k are constants that can be calibrated.

Flexure and Opto-Mechanical System Design

A flexure is an elastic component that converts external force to mechanical deformation. Based on the FPI fiber sensor (FOS-N-BA-C1-F1-M2-R1-ST, FISO Technologies, Inc., Canada), we designed a flexure mechanism built from aluminum alloy 6061 (Young's Modulus 69 GPa). The FPI strain sensor is embedded vertically inside the sensor groove (the green portion shown in Fig. 3a). Two screw mounts couple the robot with the flexure. To induce strain, the flexure design incorporates a strain enhancement groove. Two piezoelectric motor fixture slots are used to constrain the piezoelectric motor drive rods. As shown in Fig. 3b, Finite Element Analysis (FEA) confirms that under a 20-N bending force, the maximum strain is within the tolerable range of the FPI sensor.

To reduce the size and cost of our first iteration of the opto-mechanical system,[20] we developed a portable system, as shown in Fig. 4. The detailed design can be found in Ref. 17.

Sensor calibration was conducted by adding known incremental weights to the FPI sensor flexure along the needle insertion direction. The calibration relationship between force and output voltage is characterized as:

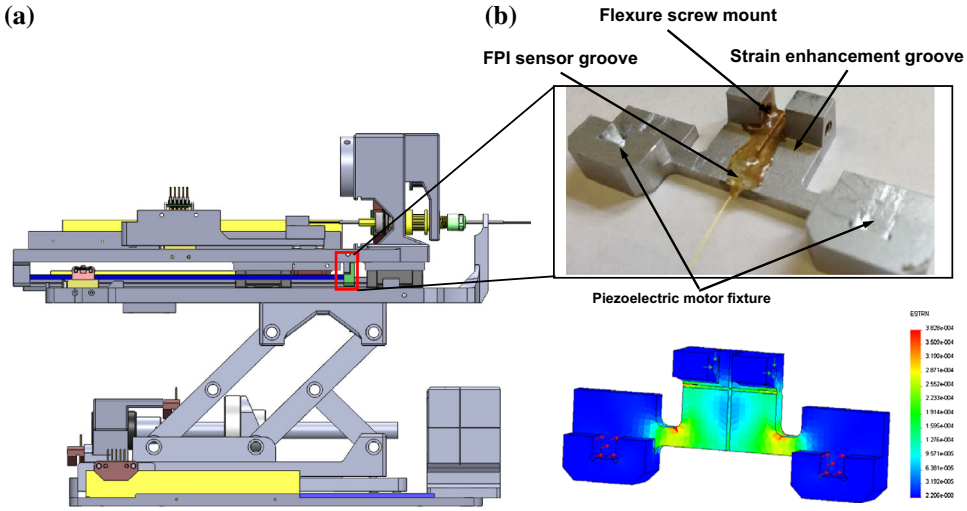

FIGURE 3. (Left) A flexure with FPI force sensing was integrated with the slave robot . (Right) The inlet shows the flexure design and FPI fiber sensor element embedded inside the sensor groove. The FPI sensor element was placed vertically on the surface of the flexure.

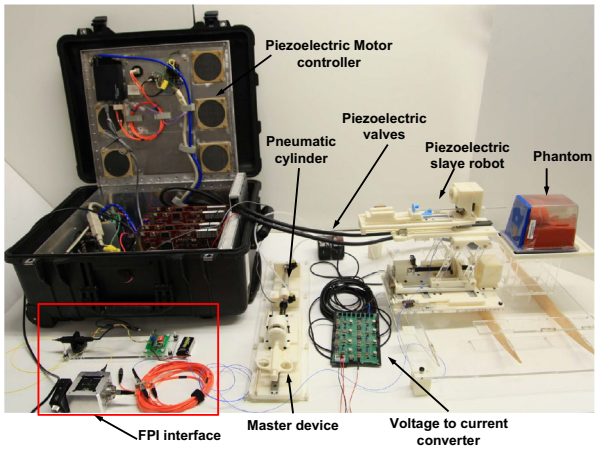

FIGURE 4. The telesurgery system consisting of a piezoelectric slave robot with FPI force sensing and a pneumatic haptic device with strain gauge force sensing as the master robot.

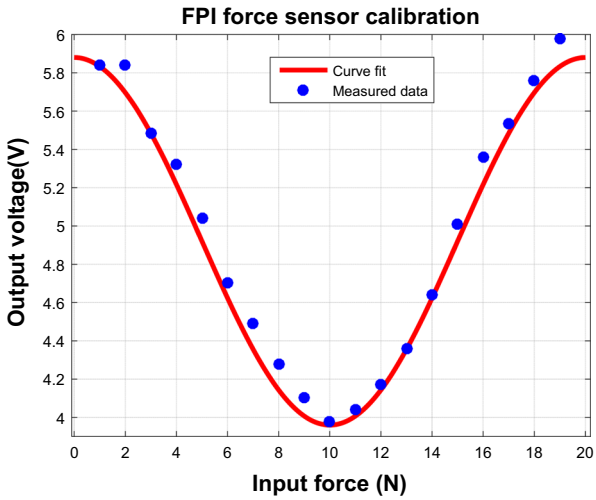

FIGURE 5. FPI sensor force voltage calibration result.

$$u = 0.96\cos(0.31f - 0.02) + 4.92$$

where f is the force and u is the measured voltage. The relation between the known weight and the sensor reading was recorded for those sampling points. The force error is defined as the difference between the known weight and the calibrated force reading from FPI sensor. Then the root mean square (RMS) error between measured and actual force was calculated as 0.32 N (Fig. 5).

Pneumatic Haptic Device with Strain Gauge Force Sensing

In contrast to flow rate-controlled pneumatic systems, we used a pair of high speed piezoelectric pressure valves (PRE-I, Hoerbiger, Germany) to control the cylinder output force. Figure 8 illustrates the system schematic. This valve has a 10 ms response time with a linear relationship between the pressure and control current (2 mA/bar). A linear voltage to current conversion circuit was designed to regulate the 0–48 V analog output from the piezoelectric motor controller to the desired valve control current. Two pressure sensors (PX309-100G5V, Omega, USA) were used to measure the chamber pressures. All of the valves, the circuit board, and the pressure sensors were enclosed inside the controller box located in the scanner room to minimize the hose length and to reduce the cylinder response time. An MRI-compatible air hose (MRI-AH1200202, WT Farley Inc. USA) with a 10 mm inner diameter and 800 PSI burst pressure was applied as the interface with the medical air supply (approximately 40 PSI pressure) inside the MRI scanner room. An aluminum load cell with integrated strain guages (MLP-10, Transducer Techniques, USA) measures the interaction force between the user and the biopsy needle for closed-loop force control.

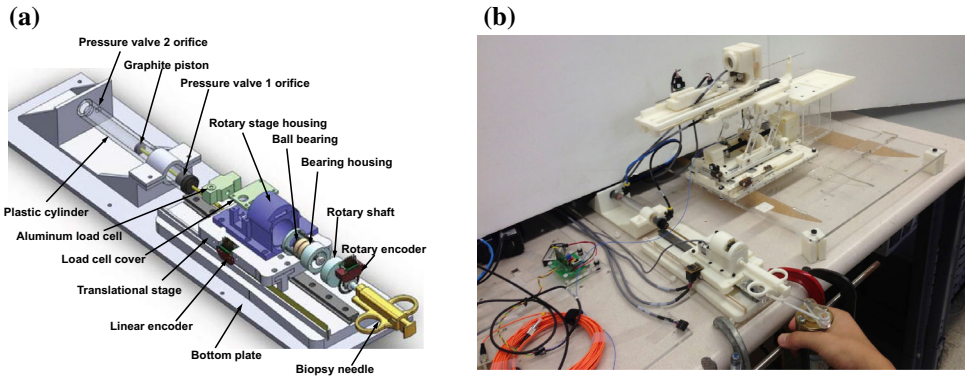

FIGURE 6. CAD model of the pneumatic haptic master device (a)[18] and prototype (b). An aluminum load cell with integrated strain gauges measures the interaction force between the user and the 3D printed biopsy needle handle.

As shown in Fig. 6, the haptic device has 2 decoupled DOF, namely, the pneumatically actuated translational DOF for insertion force rendering and the passive rotational DOF measurement for needle steering control. The bearing housing follows the rotation motion of the biopsy needle interface while the inner ring of the ball bearing remains stationary but transmits the insertion force exerted by the translation module to the pneumatic cylinder. Two angular contact ball bearings (Igus, Inc., East Providence, RI, USA) are placed against each other to ensure axial stability.

Force and Position Control of the Master-Slave Telesurgery System

With the aforementioned hardware, the control system plays an essential role in ensuring the bilateral tracking performance of the telesurgery system. An impedance control strategy was developed to ensure transparency of the haptic feedback and the stability of the overall system.

Slave Robot Position Tracking Control

After the operator selects the target point inside the MRI volume, the robot controller calculates the inverse kinematics to autonomously align the needle. The control task commands the slave robot to track the master robot needle insertion and rotation motion. The proportional integral derivative (PID) controller is position tracking error based and is linear within a confined range of position error.[19] The piezoelectric motors (PiezoLegs, LL1011C, PiezoMotor AB, Sweden) have high bandwidth and low inertia. The proportional control term was tuned to the maximum, allowing the motor to run at the fastest speed until the motor position is in close proximity to the target. The derivative damping control term is typically not significant because the piezoelectric motor exhibits overdamped dynamics, and the integral term is typically not used for dynamic tracking. Both master and slave position servo loops operate at frequency of 1 KHz.

In the motion tracking experiment, a user manipulated the haptic device with a translational range with in 77 mm, and the positions of both the master and slave robots were recorded at 200 Hz. As shown in Fig. 7, the overall position RMS error between the master and slave positions was 0.11 mm. The maximum tracking speed during this test was 7.62 mm/s.

Master Robot Force Tracking Control

On the master side, the control algorithm renders proprioception force to match the tissue insertion force measured by FPI force sensor of the slave robot. Since it is challenging to ensure high-fidelity force display of a pneumatic haptic device, the electromechanical design of the haptic device incorporates four features to ameliorate nonlinearity issues. (1) The high bandwidth

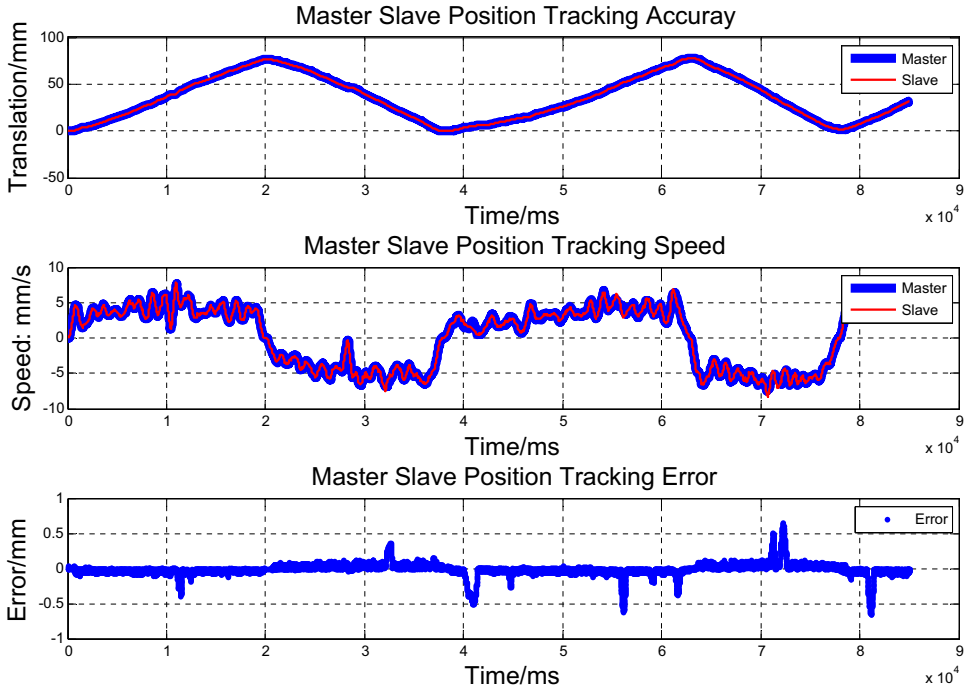

FIGURE 7. Representative teleoperation results of slave robot position tracking, speed and error trajectory. The slave robot tracks the master robot motion for 85 s with 0.11 mm RMS error.

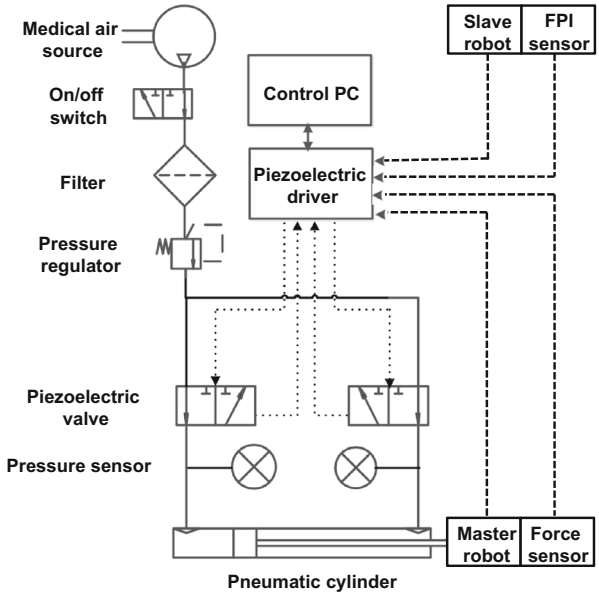

FIGURE 8. Pneumatic diagram of the master haptic device. Two piezoelectric valves regulates the differential pressure inside the two chambers of the air cylinder.

piezoelectric pressure regulation valve has a 10 ms response time with a linear relationship between the pressure and control current. This facilitates high bandwidth response of the control system; (2) Two pressure sensors were used to measure the chamber pressures for closed-loop force control; (3) The pneumatic cylinders are MRI-compatible and produce low friction force (as low as 0.01 N) as the cylinder bore is made of glass and the piston and seals are made of graphite; and (4) the setup to place the control system in the scanner room enables ensures short pneumatic hoses to reduce delay. The paper focuses on needle insertion force display using this haptic device and the needle insertion process is considered to be with limited acceleration, thus the haptic interaction with the surgeon is not modeled in this paper.

In the bench-top test, a user held the master robot biopsy needle, and the master robot was commanded to track a sinusoidal force with a 20 N magnitude to simulate the FPI force sensing. As shown in Fig. 8, the pressure force generated by the opposing pair of piezoelectric valves is

$$F_p = P_1 A_1 - P_2 A_2$$

where P_1 and P_2 are the respective pressures of the two chambers, and A_1 and A_2 are the respective piston areas. For the desired control force F_d, the desired pressure of each valve is calculated as follows:

If $F_d \geq 0$,

$$\begin{cases} P_1^d = \frac{1}{A_1}(F^d + P_{20}A_2) \\ P_2^d = P_{20} \end{cases}$$

If $F_d < 0$,

$$\begin{cases} P_1^d = P_{10} \\ P_2^d = -\frac{1}{A_2}(F^d - P_{10}A_1) \end{cases}$$

where P_{10} and P_{20} are the initially set pressures of the two chambers.

To evaluate the accuracy and bandwidth of the pneumatic haptic device force tracking, the pneumatic haptic device was commanded to track a chirp signal (time varying frequency). The reference chirp force signal is defined as $F^d = a\sin(2\pi ft) + b$, where $a = 7$, $b = 9$, $f = 0.01t$, and t is the time variable. Figure 9 demonstrates the Bode plot of the master robot force tracking and the tracking bandwidth is identified as 5.5 Hz at -3 dB. We have also shown the preliminary force tracking of 1 Hz sinusoidal force signal in our previous work[18] In comparison, the MRI-compatible pneumatic actuators presented similar force tracking accuracy performance but at a much lower bandwidth (0.1 Hz).

RESULTS

The image quality during the piezoelectric slave robot operation was previously studied in Ref. 19. With the addition of the FPI sensor (inside the MRI scanner bore) and the pneumatic haptic device (inside the scanner room), the first objective of the present experiments was to evaluate the MRI compatibility of the telesurgery system. The second objective was to understand the teleoperated needle placement capability of the master-slave system.

Quantitative Evaluation of Robot-Induced Image Interference

The effects of this device on the MR image quality were evaluated using the following two methods: 1) Signal-to-Noise Ratio analysis based on the National Electrical Manufacturers Association (NEMA) standard MS1-2008[15] and 2) Geometric distortion analysis based on the NEMA standard (MS2-2008).[14]

The experiments were conducted with a 3-Tesla closed-bore MRI scanner (Achieva, Philips, Netherlands) using a Periodic Image Quality Test (PIQT) phantom (Philips, Netherlands), as shown in Fig. 12. The phantom has complex geometric features, including cylindrical cross section, arch and pin section. To mimic the clinical scenario, the robot was placed 5 mm away from the phantom. The controller was placed approximately 2 m away from the scanner bore inside the scanner room (Fig. 10).

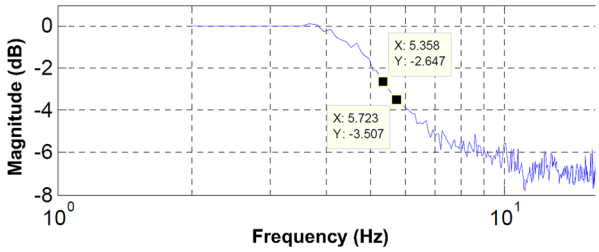

FIGURE 9. Bode plot of the master robot force tracking and the tracking bandwidth is identified as 5.5 Hz at −3 dB.

FIGURE 10. The master slave teleoperation system setup with a Philips Achieva 3 Tesla MRI scanner.

Signal-to-Noise Ratio Based Compatibility Analysis

Four imaging protocols typically used in prostate imaging were used to study the SNR properties of the phantom images: (a) T1-weighted Fast Field Echo (T1W-FEE) with fat selective pulse for fiducial imaging (i.e., *Z*-frame[19]), (b) T2-weighted 2D Turbo Spin Echo for initial scan (T2WTSE-Init), (c) T2-weighted 2D Turbo Spin Echo for needle conformation image (T2W-TSENeedle), and (d) Balanced FFE sequence (TFE-RTCircle) for real-time imaging for needle guidance. The detailed parameter settings for each protocol are documented in Ref. 17.

Following the NEMA standard,[15] the SNR was calculated as the mean signal in the center of the phantom divided by the noise outside the phantom. Mean signal is defined as the mean pixel intensity in the region of interest. The noise is defined as the average mean signal intensity in the four corners divided by 1.25.[15]

Nine configurations of the robot were assessed to identify the root cause of image quality degradation[17] including baseline, baseline again, robot only, robot and controller (not powered), robot and controller (not powered) again, Robot and controller (Powered, E-stop ON), controller (powered, E-stop OFF), simultaneous robot motion and imaging, and baseline again.

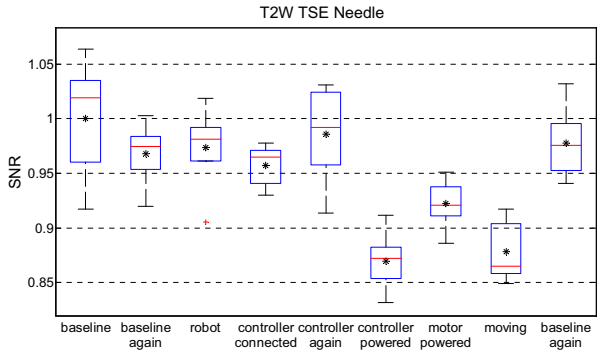

FIGURE 11. Normalized SNR boxplot of each configuration with the T2W TSE Needle protocol. The most significant decrease of SNR is in configuration "moving" with a 16.8% SNR drop compared with the baseline.

Figure 11 depicts the statistical result of the T2W TSE Needle protocol in nine configurations, and each configuration analyzed five images. The SNR was normalized to the mean SNR of the first baseline configuration. In each boxplot, the black asterisk is the average, and the red central line is the median. The edges of the box are the 25th and 75th percentiles. The results show an average 5% decrease in the SNR in the first five configurations and an average 14% drop in configurations 6–8. The most significant decrease is in configuration "moving" with a 16.8% SNR drop compared with the baseline. This result of teleoperation system consisting of an FPI sensor, a 6-DOF slave robot, and a 2-DOF haptic device is better than the 1-DOF robot system.[4] Reference 4 had a 26% SNR reduction with visually observable artifacts.

Geometric Distortion Analysis

The NEMA standard (MS2-2008)[14] defines 2D geometric distortion as the maximum percent difference between the measured distances in an image and the actual corresponding phantom dimensions. Eight pairs of radial measurements (i.e., between points spanning the center of the phantom) were used to characterize the geometric distortion for the four protocols as shown in Fig. 12. A numerical table comparison of all configurations was reported in Ref. 17.

MR image analysis indicates that (1) because the distortion results for 3 baseline configurations were on the same level, the environment did not change during the experiment, and thus the analysis was reliable. (2) the maximal distortions for all configurations under the four protocols were less than 1%. This analysis demonstrates negligible geometric distortion of the acquired images even during robot operation with simultaneous imaging.

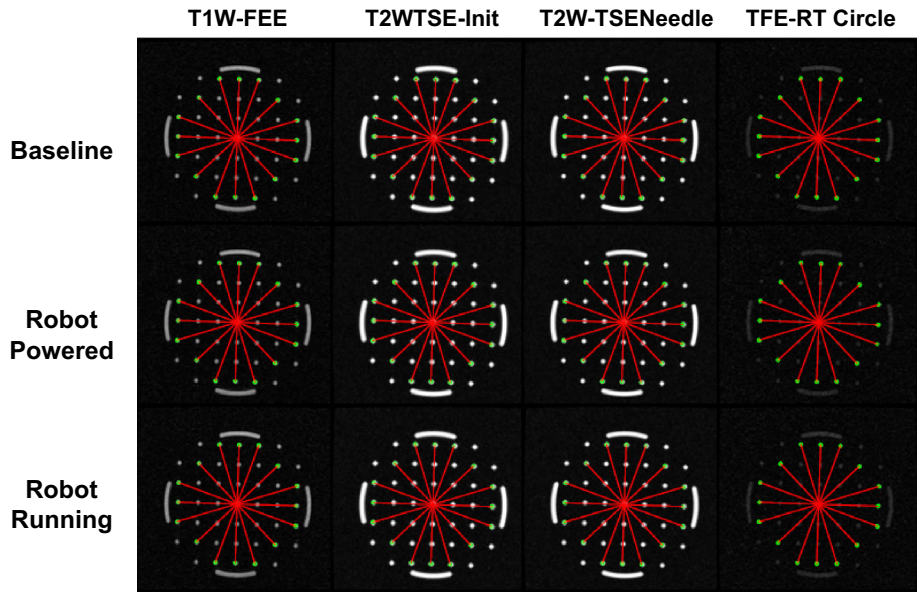

FIGURE 12. MR images for distortion analysis with four prostate imaging protocols in baseline, robot powered and robot in motion configurations.

Teleoperated Needle Insertion Under Live MRI

One of the key objectives of this work is to demonstrate the capability of manual control of the translation and rotation motion of the haptic device to steer a bevel-tipped flexible needle to reach targets inside a phantom model. A tissue-mimicking phantom made from 10% (by weight) Knox gelatin (Kraft Foods Global Inc., USA) was molded into a 10 cm × 10 cm × 15 cm rectangular form. Three rods with ellipsoidal heads made from acrylonitrile butadiene styrene (ABS) using a 3D printer (Dimension, Stratasys Inc., USA) were placed horizontally inside the phantom to simulate the target and obstacles. A bevel-tipped flexible nitinol needle (0.7 mm diameter, 22G) and a tip angle of 30° were used. The teleoperation task was designed to mimic a prostate biopsy procedure in which the ellipsoidal head (a) in Fig. 13 simulated the suspicious tumor. The ellipsoidal head (c) is an obstacle to be avoided because it has been observed clinically that the pubic arch might block the needle insertion trajectory. The ellipsoidal head (b) mimicked an tissue to be avoided. The targets were manually selected from the MRI images on the edge of the ellipsoidal head (a).

Figure 13 illustrates the control strategy and teleoperation results. To avoid the obstacle, the needle was turned 180° clockwise before insertion. During the first portion of the insertion, while the needle was inserted with relatively constant speed, it was rotated by the user based on visual feedback to avoid the obstacle. Once the needle passes the obstacle ellipsoid (a), it was rotated by 180° counter clockwise to steer towards the target ellipsoid (b). Figure 14 illustrates the joint level tracking results corresponding to Fig. 13, demonstrating 0.32 mm translational RMS error and 0.4° rotational RMS error. The teleoperated needle placement procedure with obstacle avoidance took approximately 4 min. The targets for the teleoperation obstacle avoidance demonstration were at the edge of the needle tip as shown in Fig. 13.

To demonstrate the haptic force display, a user controlled the pneumatic haptic device to teleoperate the needle insertion of the slave robot. The result of one representative trial of the insertion and retraction process is shown in Fig. 15 with three phases: fast insertion of the haptic device, slave robot stall motion, and fast retraction of the haptic device. The blue and red lines indicate the position of the master and slave robots respectively. The green line indicates the force displayed to the user. In the first phase (fast insertion of the haptic device), in the time interval between 32 and 60 s, the master robot was inserted faster than the speed at which that slave could move. Thus the haptic device applied resistive force to the user to restrict the fast needle insertion. In the second phase (slave robot stall motion), at approximately 60 s, the slave robot reached the 60 mm insertion limit and stopped the insertion motion while the master was still being inserted by the user. As the result of the impedance control, haptic device displayed resistive force to prevent the user's insertion. In the third phase (fast retraction of the haptic device), at approximately 80 s, the force feedback has also successfully restricted the fast movement of the haptic device during the needle retraction.

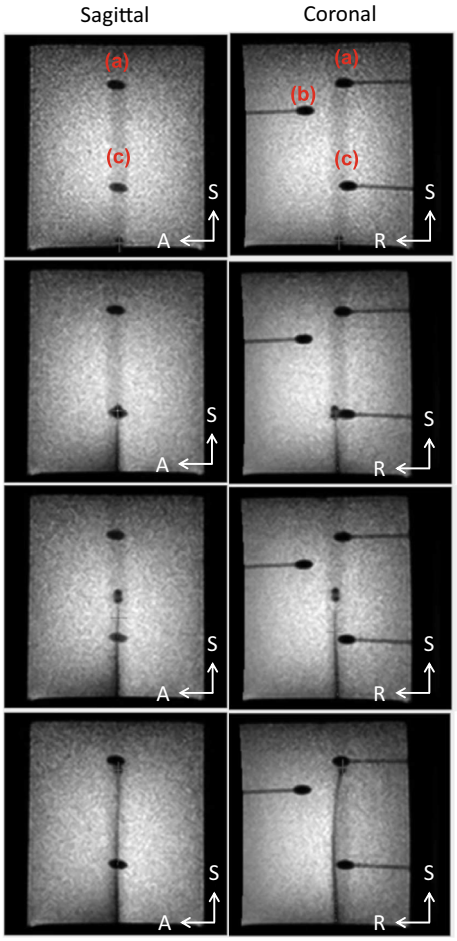

FIGURE 13. Incremental images from the 2-DOF teleoperated needle steering in the sagittal (left) and coronal (right) planes. (a) is the tumor mockup, (b) mimics an tissue to be avoided, and (c) is an obstacle to be avoided, similar to a pubic arch that might block insertion trajectory. The teleoperated needle successfully avoided the obstacle and reached the tumor.

To further study the reliability and repeatability of this teleoperation system, 10 teleoperated needle placement procedures were conducted with continuous MRI guidance. A closed-loop asymmetric-tip needle tracking and steering method[16] was developed and utilized for continuous intraoperative MRI guidance and control. The 10 teleoperated needle placement procedures (without obstacle avoidance) took about 3–5 min on average. The offset distances (lateral steering distance) between the center line and the targets for the 10 teleoperated needle placement procedures are approximately 11 mm depending on the location of the target on the edge of the target sphere.

For the 10 needle placement trials, the errors along the axes of the Right, Anterior, Superior (RAS) coordinate system, the in plane (the plane defined by the Right-Anterior axes) errors and Cartesian errors are shown in Fig. 16. Quantitatively, the needle

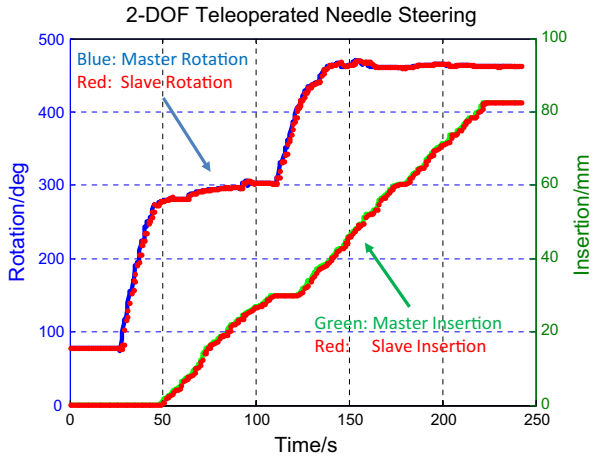

FIGURE 14. Translational and rotational joint positions measurement of the master and slave robots showing accurate tracking performance. The translational RMS error was 0.32 mm and rotational RMS error was 0.4°. The needle was rotated by 180° clockwise before insertion, and was rotated by 180° counter clockwise to steer towards the target ellipsoid (c).

placement error in Cartesian space (Euclidean distance between the desired and actual needle tip) for the 10 targets was 0.70 ± 0.35 mm. In the experiments, the error in the insertion direction (superior axis) was insignificant because it could be compensated with future insertion adjustment. As shown in the coronal plane of Fig. 13, the two small blobs at the end of the needle are needle tip artifacts (most likely due to the geometry of the needle tip in the homogeneous field B_0), which introduced extra error into the actual tip position localization. Therefore, the in-plane error (RA plane, 0.69 ± 0.35 mm) is more practically important.

DISCUSSION

This paper presents a surgical master-slave teleoperation system for percutaneous interventional procedures under continuous MRI guidance. The insertion and rotation motion of the slave robot was controlled by teleoperation. Alternatively, the rotational DOF of the slave robot can be controlled by closed-loop image feedback, as demonstrated in our prior work.[16] Due to the nature of the closed-loop motion control, this procedure might simplify the needle steering procedure while enhancing the targeting accuracy. A clinical-grade variant of the described slave robot based on the same control system is currently in clinical trials at the Brigham and Womens Hospital, Harvard Medical School.[5] It is expected that the teleoperation system would represent the next phase of our clinical effort to

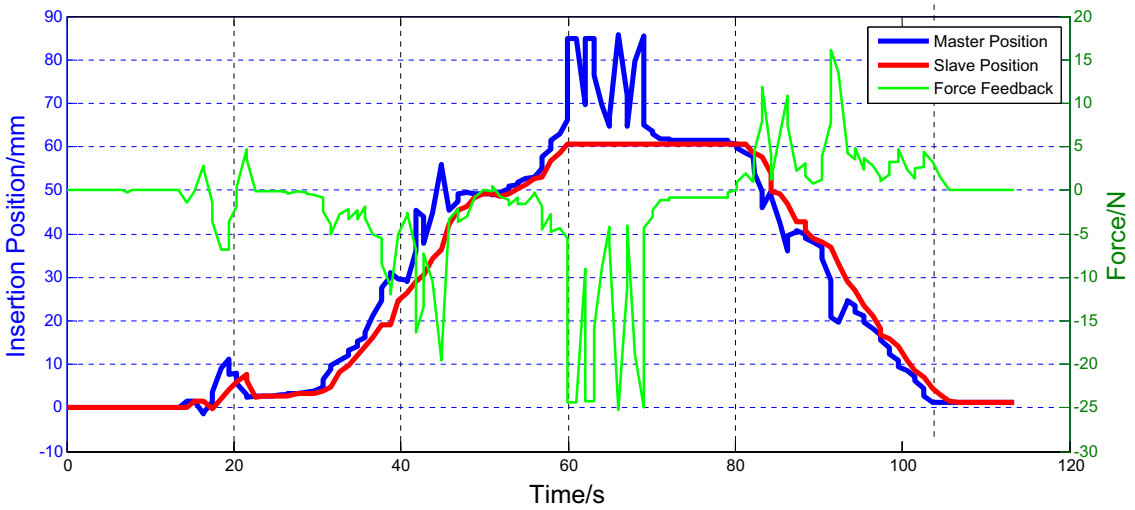

FIGURE 15. The position and force trajectory in a teleoperation experiment where the slave robot was teleoperated by the master robot (pneumatic haptic device). This demonstrates the three phases of the teleoperation: fast insertion of the haptic device (between 32 and 60 s), slave robot stall motion (between 60 and 80 s), and fast retraction of the haptic device (between 80 and 105 s). The insertion depth limit is 60 mm. The blue line indicates the master robot insertion depth (1 DOF), the red line indicates the slave robot insertion depth (1 DOF) and the green line indicates the force displayed to the user using the master robot.

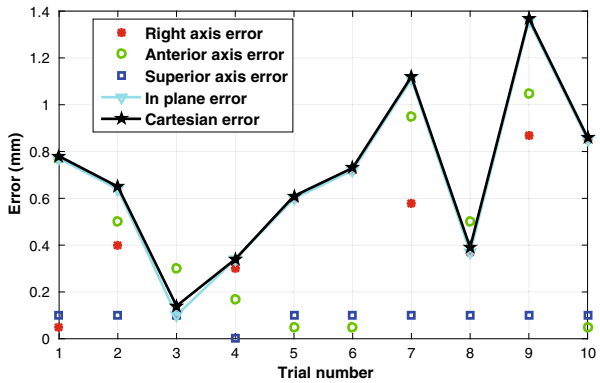

FIGURE 16. Accuracy assessment of MRI-guided closed-loop needle placement for 10 targets inside an tissue-mimicking phantom. This shows the the errors along the RAS axes, the in plane errors (excluding the error along superior axis) and the errors in Cartesian space. The error is bounded in 1.5 mm range for the 10 trials.

further explore its potential for reducing procedure time and ensuring accuracy.

ACKNOWLEDGMENTS

This work is supported in part by the Congressionally Directed Medical Research Programs Prostate Cancer Research Program New Investigator Award W81XWH-09-1-0191, NIH Bioengineering Research Partnership 1R01CA111288-01A1, and Link Foundation Fellowship in Advanced Simulation and Training.

REFERENCES

[1]Cepek, J., U. Lindner, S. Ghai, A. S. Louis, S. R. Davidson, M. Gertner, E. Hlasny, M. S. Sussman, A. Fenster, and J. Trachtenberg. Mechatronic system for in-bore MRI-guided insertion of needles to the prostate: an in vivo needle guidance accuracy study. *J. Magn. Reson. Imaging* 42(1):48–55, 2015.

[2]Chinzei, K. and K. Miller. Towards MRI guided surgical manipulator. *Med. Sci. Monit.* 7(1):153–163, 2001.

[3]Comber, D. B., E. J. Barth, and R. J. Webster. Design and control of an magnetic resonance compatible precision pneumatic active cannula robot. *J. Med. Dev.* 8(1):011003, 2014.

[4]Elhawary, H., A. Zivanovic, M. Rea, B. Davies, C. Besant, D. McRobbie, N. de Souza, I. Young, and M. Lamperth. The feasibility of MR-image guided prostate biopsy using piezoceramic motors inside or near to the magnet isocentre. *Med Image Comput Comput Assist Interv* 9(Pt 1):519–526, 2006.

[5]Eslami, S., W. Shang, G. Li, N. Patel, G. S. Fischer, J. Tokuda, N. Hata, C. M. Tempany, and I. Iordachita. In-bore prostate transperineal interventions with an MRI-guided parallel manipulator: system development and preliminary evaluation. *Int. J. Med. Robot. Comput. Assist. Surg.* 12:199–213, 2015.

[6]Felfoul, O., A. Becker, C. Bergeles, and P. E. Dupont. Achieving commutation control of an MRI-powered robot actuator. *IEEE Trans. Robot.* 31(2):387–399, 2015.

[7]Gangopadhyay, T. K. Prospects for fiber Bragg gratings and Fabry-Perot interferometers in fibre-optic vibration sensing. *Sens. Actuators A* 113(1):20–38, 2004.

[8]Ho, M., A. McMillan, J. Simard, R. Gullapalli, and J. Desai. Toward a SMA-actuated MRI-compatible neurosurgical robot. *IEEE Trans. Robot.* 28(1):213–222, 2012.

[9]Kokes, R., K. Lister, R. Gullapalli, B. Zhang, A. MacMillan, H. Richard, and J. P. Desai. Towards a teleoperated needle driver robot with haptic feedback for RFA

of breast tumors under continuous MRI. *Med. Image Anal.* 13(3):445–455, 2009.

[10]Krieger, A., S. Song, N. Bongjoon Cho, I. Iordachita, P. Guion, G. Fichtinger, and L. L. Whitcomb. Development and evaluation of an actuated MRI-compatible robotic system for MRI-guided prostate intervention. *IEEE/ASME Trans. Mechatron.* (99):1–12, 2012.

[11]Li, G., H. Su, G. Cole, W. Shang, K. Harrington, A. Camilo, J.G. Pilitsis, and G. S. Fischer. Robotic system for MRI-guided stereotactic neurosurgery. *IEEE Trans. Biomed. Eng.* 62(4):1077–1088, 2015.

[12]Li, M., A. Kapoor, D. Mazilu, and K. Horvath. Pneumatic actuated robotic assistant system for aortic valve replacement under MRI guidance. *IEEE Trans. Biomed. Eng.* 58(2):443–451, 2011.

[13]Nathoo, N., M. Çavusoglu, M. Vogelbaum, and G. Barnett. In touch with robotics: neurosurgery for the future. *Neurosurgery* 56(3):421, 2005.

[14]NEMA. Determination of image uniformity in diagnostic magnetic resonance images. NEMA standards publication MS 3-2008.

[15]NEMA. Determination of signal-to-noise ratio (SNR) in diagnostic magnetic resonance imaging. NEMA standard publication MS 1-2008.

[16]Patel, N. A., T. van Katwijk, G. Li, P. Moreira, W. Shang, S. Misra, and G. S. Fischer. Closed-loop asymmetric-tip needle steering under continuous intraoperative MRI guidance. In: 37th Annual International Conference of the IEEE Engineering in Medicine and Biology Society (EMBC), pages 4869–4874. IEEE, 2015.

[17]Shang, W. Teleoperation of MRI-Compatible Robots with Hybrid Actuation and Haptic Feedback. PhD thesis, Worcester Polytechnic institute, 2014.

[18]Shang, W., H. Su, G. Li, and G. S. Fischer. Teleoperation system with hybrid pneumatic-piezoelectric actuation for MRI-guided needle insertion with haptic feedback. In: 2013 IEEE/RSJ International Conference on Intelligent Robots and Systems, pp. 4092–4098. IEEE, 2013.

[19]Su, H., W. Shang, G. Cole, G. Li, K. Harrington, A. Camilo, J. Tokuda, C. M. Tempany, N. Hata, and G. S. Fischer. Piezoelectrically-actuated robotic system for MRI-guided prostate percutaneous therapy. *IEEE/ASME Trans. Mechatron.* 99(3):1–13, 2015.

[20]Su, H., M. Zervas, G. Cole, C. Furlong, and G. S. Fischer. Real-time MRI-guided needle placement robot with integrated fiber optic force sensing. In: IEEE ICRA International Conference on Robotics and Automation, 2011.

[21]Tilak, G., K. Tuncali, S.-E. Song, J. Tokuda, O. Olubiyi, F. Fennessy, A. Fedorov, T. Penzkofer, C. Tempany, and N. Hata. 3T MR-guided in-bore transperineal prostate biopsy: a comparison of robotic and manual needle-guidance templates. *J. Magn. Reson. Imaging* 42(1):63–71, 2015.

[22]Tse, Z., H. Elhawary, M. Rea, B. Davies, I. Young, and M. Lamperth. Haptic needle unit for MR-guided biopsy and its control. *IEEE/ASME Trans. Mechatron.* 17(1):183–187, 2012.

[23]Yakar, D., M. G. Schouten, D. G. H. Bosboom, J. O. Barentsz, T. W. J. Scheenen, and J. J. Futterer. Feasibility of a pneumatically actuated MR-compatible robot for transrectal prostate biopsy guidance. *Radiology* 260(1):241–247, 2011.

[24]Yang, B., S. Roys, U.-X. Tan, M. Philip, H. Richard, R. P. Gullapalli, and J. P. Desai. Design, development, and evaluation of a master-slave surgical system for breast biopsy under continuous MRI. *Int. J. Robot. Res.* 33:616–630, 2013.

[25]Yang, B., U.-X. Tan, A. B. McMillan, R. Gullapalli, and J. P. Desai. Design and control of a 1-DOF MRI-compatible pneumatically actuated robot with long transmission lines. *IEEE/ASME Trans. Mechatron.* 16(6):1040–1048, 2011.

[26]Yu, Y., T. K. Podder, Y. D. Zhang, W. S. Ng, V. Misic, J. Sherman, D. Fuller, D. J. Rubens, J. G. Strang, R. A. Brasacchio, and E. M. Messing. Robotic system for prostate brachytherapy. *Comput. Aided Surg.* 12(6):366–370, 2007.